energies

MDPI

Article

Tolerance Sensitivity Analysis and Robust Optimal Design Method of a Surface-Mounted Permanent Magnet Motor by Using a Hybrid Response Surface Method Considering Manufacturing Tolerances

Cha-Seung Jun [1,*], Byung-Il Kwon [2,*] and Ohbong Kwon [3]

1 Appliance R & D Laboratory, LG Electronics Inc., Seoul 08592, Korea
2 Department of Electronic Systems Engineering, Hanyang University, Ansan 15588, Korea
3 New York City College of Technology, New York 11201, NY, USA; okwon@citytech.cuny.edu
* Correspondence: xdori71@naver.com (C.-S.J.); bikwon@hanyang.ac.kr (B.-I.K.); Tel.: +82-31-400-5165 (B.-I.K.)

Received: 9 April 2018; Accepted: 3 May 2018; Published: 5 May 2018

Abstract: This paper presents a robust optimal design method using a hybrid response surface method (H-RSM) which directly finds an optimal point satisfying a target Z-value or a probability of failure. Through three steps, this paper achieves the goal that is to increase the open-circuit airgap flux (OCAF) in a surface-mounted permanent magnet motor and decrease its variation caused by variations of the airgap lengths including an additional one between permanent magnets and rotor back yoke. First, the OCAF equation is derived from the magnetic equivalent circuit (MEC) considering the additional airgap. Then, the equation is validated by comparing its results with those of the finite element method (FEM) modeled by the slotless stator. Next, the tolerance sensitivity analysis, using the partial derivative of the OCAF equation with respect to the airgap length, is performed to investigate the effects of design variables on the OCAF. It is shown that increasing the magnet thickness is effective for both increasing mean of the OCAF and reducing its variation. Finally, robust optimal design is performed using the H-RSM, in which all data are obtained from the FEM modeled by the slotted stator. The results of the robust optimal design are verified using the FEM.

Keywords: hybrid response surface design; manufacturing tolerance; robust design; surface-mounted permanent magnet (SPM) motor; Taguchi robust design

1. Introduction

Achieving high efficiency in electrical machines is important to meet increased energy standards while preserving the environment. In order to increase motor efficiency, new topologies and manufacturing methods for electric motors have been developed by motor engineers.

Nevertheless, the conventional surface-mounted permanent magnet (SPM) motors showing the less open-circuit airgap flux (OCAF), as compared to other permanent magnet (PM) motors, have been widely used due to their simple structure and control algorithm.

In addition, motor engineers should carry out the robust optimal design which is needed to satisfy the required probability of failure (POF) caused by the variations of the uncontrollable noise factors such as the manufacturing tolerances, the operating temperature, etc., as well as the mean value of the target performance [1].

A few previous studies have investigated how the motor performance is influenced by manufacturing tolerances in PM motors and how the robustness of PM motors can be improved, mainly in terms of the cogging torque and torque ripple.

The effectiveness of the various methods to reduce cogging torque in mass production being subject to manufacturing tolerances was validated by using the finite element method (FEM) coupled with a statistical analysis in [2–4].

The influence of additional airgaps, which is caused by the manufacturing tolerances between segmented stator cores which is used for the higher fill factor, on the cogging torque was analyzed by using the FEM or analytical solutions in [5–8].

A few groups have carried out statistical analysis of the effects of magnet tolerance such as magnet misplacement, remanence variation, etc., on the cogging torque or torque ripple by using the FEM or analytical expressions in [9–12]. In [13–19], the authors carried out the robust optimal design, using the Taguchi robust method or design of experiment and etc., to improve the variation of motor performance, e.g., cogging torque and torque ripple, caused by the manufacturing tolerances.

In [20], the authors presented a torque control scheme of a PM motor considering the OCAF variation due to the manufacturing tolerances or temperature variation of the PM, which can be used in the full operation region.

However, these references analyzed the effects of the manufacturing tolerances mostly on the variations of the cogging torque and torque ripple in SPM motors by using complicated analytical equations, FEM, and statistical analyses. So it was observed that little research had been carried out on the OCAF variation caused by the manufacturing tolerances even though the OCAF is the most fundamental and important characteristics for the high-quality motor.

In addition, the FEM used in the previous studies is time-consuming and it is difficult to physically investigate the cause and effect between design variables and the OCAF.

Guo et al. presented a system level robust optimal design to achieve two target indices i.e., mean and standard deviation of an objective function by using optimization tools, FEM, and six sigma tools [21–26].

In [27], the authors focused on the application of the variance-based global sensitivity analysis for a topological derivative method in order to solve a stochastic nonlinear time-dependent magneto-quasi-static interface problem, in which the objective is to provide a robust design of the rotor poles and of the tooth base in a stator for the reduction of the torque ripple and electromagnetic losses, while taking material uncertainties into account.

However, these methods also seem to be time-consuming and it is difficult to theoretically investigate the effects of the design variables on the OCAF. Therefore, this paper presents the robust optimal design method using a hybrid response surface method (H-RSM) which directly finds an optimal point satisfying a target Z-value or a probability of failure through three steps. The objective of the method is to achieve the six-sigma level of Z-value of the OCAF; the six-sigma level of Z-value corresponds to 0.00034% of the POF [1].

First, the OCAF of the SPM motor is analyzed using the magnetic equivalent circuit (MEC) to investigate the functional relationship between OCAF and design factors; the analytical solution solving the electromagnetic field equation can be the alternative method [28]. However, the method is difficult to study the effect of the additional airgaps and to investigate the functional relationship between OCAF and design factors, thus, the MEC method is used for the magnetic analysis in this paper.

There have been lots of studies on the MEC of the SPM motor to study more hard problems such as magnetic saturation effect and armature reaction field until recently [29–33]. However, it is difficult to find out articles studying the influence of the additional airgap between the PMs and rotor back yoke. Therefore, it is modeled in the MEC in this paper and the OCAF equation is derived from the MEC in order to investigate the effects of design variables, i.e., airgap length, magnet thickness (MT), and magnet pole angle (MPA), on the OCAF and its variation due to variations of the airgap lengths. Then, the results of the MEC method are compared with those of the FEM modeled by slotless stator to validate the results.

Second, the tolerance sensitivity analysis, using the partial derivative of the OCAF equation with respect to the airgap length, is performed to investigate the effects of design variables on the variation of the OCAF. The objective of the tolerance sensitivity analysis is to preliminarily investigate design directions of the robust optimal design before performing that. Finally, the robust optimal design using the H-RSM is carried out to achieve the six-sigma level of Z-value on the OCAF, in which motor characteristics are analyzed using the FEM modeled by slotted stator.

2. Tolerance Sensitivity Analysis of the OCAF Using MEC Considering the Manufacturing Tolerances

2.1. Analysis Model Using MEC

The OCAF Φ_g is one of the most important characteristics for analyzing and designing PM motors and their control strategies. Thus, it is necessary to study the OCAF from the initial design stage to the optimization stage in detail.

In this paper, the OCAF and its variation caused by variations of the airgap lengths, including the additional airgap between the PMs and the rotor back yoke, are investigated based on the MEC method and its analytical equation in order to explicitly study the functional relationship between design variables and the effective OCAF. Table 1 shows the specifications of analysis model in this paper.

Table 1. Specifications of analysis model.

Item	Unit	Value
Slots/Poles	-	9/6
Winding	-	Concentrated
Serial turns per phase	-	480
Stator outside radius	mm	53
Stator inside radius	mm	30.6
Rotor outside radius	mm	30.0
Stack length	mm	35
Stack length	mm	35
Core material	mm	50JN1300
Magnet material	-	Ferrite (Br 0.42T)
Magnet thickness	mm	9.0
Rated torque	N-m	0.5
Rated speed	rpm	2850
DC link voltage	V	310

Figure 1 shows the analysis model which is composed of the fractional-slot concentrated winding (FSCW) with nine slots in the stator and the SPM with six poles in the rotor. To simplify the analysis and to investigate the trends of the effective OCAF according to the design variables, the slotted stator core in Figure 1a is replaced with the slotless stator core and it is mathematically expressed by the carter coefficient K_c [29–32]. In addition, the magnetic saturation effect occurred in the electrical steel is not considered in this MEC, assuming the SPM motor does operate in the linear permeability region at the open-circuit condition.

There can be two additional airgaps in the stator and rotor. One is the additional airgap between segments of the stator cores which has been used for increasing the slot fill factor and the other is that between the PMs and rotor back yoke; these are represented by A and B in Figure 1, respectively. The two additional airgaps result in a decrease in the OCAF and motor performance; thus, they should be included in the MEC model.

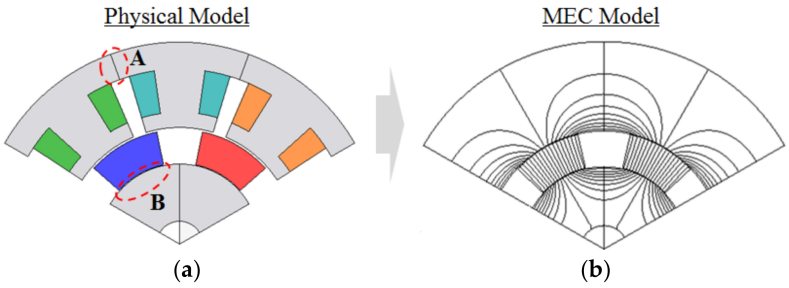

Figure 1. Analysis model: (**a**) Physical model; (**b**) Analysis model for magnetic equivalent circuit (MEC).

2.2. Analysis of the OCAF Using MEC

Effects of the additional airgaps A and B in Figure 1 are considered in the MEC and its derived equations. The additional airgaps A and B in Figure 1 are expressed as l_{cg} and l_{mg}, respectively, in Figure 2a which is the equivalent linear model of the SPM motor in this paper.

Figure 2b shows the initial full MEC with the ring-type stator core, in which the magnetic reluctance accounting for the additional airgap l_{cg} in the stator core can be considered to be included in the stator core reluctance R_{sc} and the magnetic reluctance accounting for the additional airgap l_{mg} is expressed by R_{mg}.

The initial MEC model depicted in Figure 2b can be simplified as shown in Figure 2d. The simplification procedure was explained in [25] in detail, so, only different points are presented in this paper.

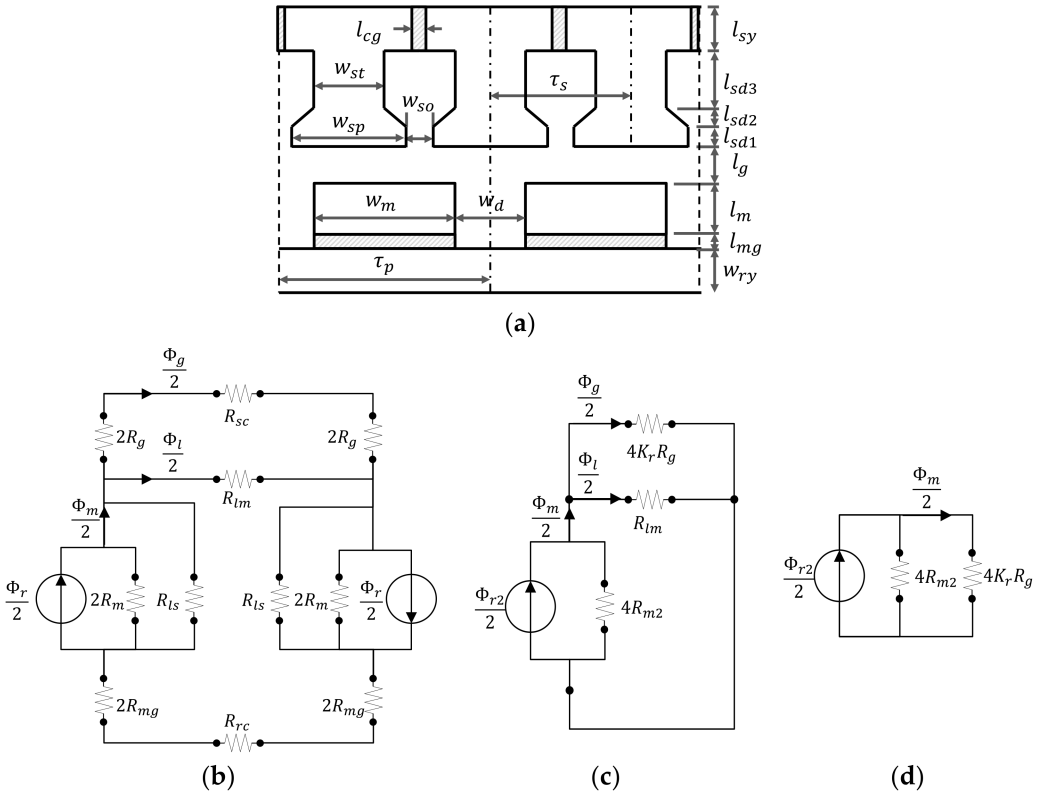

Figure 2. Analysis model and its magnetic equivalent circuit (MEC) including additional airgaps: (**a**) Equivalent linear model of the SPM motor; (**b**) Initial full MEC; (**c**) First simplified MEC; (**d**) Final Simplified MEC.

Table 2 shows all of the elements used in the MEC in Figure 2b. R_{ls} and R_{rc} are ignored due to their relatively small effects on the OCAF. The effect of R_{mg} can be included in the PM model by Equations (1) and (2):

$$R_{m2} = R_m + R_{mg} \tag{1}$$

$$\Phi_{r2} = \frac{R_m}{R_{m2}} \Phi_r \tag{2}$$

R_{sc} is combined with R_g and expressed by the reluctance coefficient K_r written in Equation (3) [29]. In this paper, R_{sc} includes the additional airgap l_{cg} between the segmented stator cores, so the value of the reluctance would be larger than that not including the additional airgap:

$$K_r = \frac{R_{sc} + 4R_g}{4R_g} \tag{3}$$

Table 2. Magnetic reluctance and flux used in the Figure 2b.

Element	Description
R_{sc}	stator core
R_g	Airgap
R_{lm}	PM mutual-leakage
R_m	PM
R_{ls}	PM self-leakage
R_{mg}	PM additional airgap
R_{ry}	Rotor core
R_{m2}	$R_m + R_{mg}$
Φ_g	OCAF
Φ_{ls}	Self-leakage flux of PM
Φ_{lm}	Mutual-leakage flux of PM
Φ_r	Residual flux of the PM
Φ_{r2}	Residual flux of PM including effect of the R_{mg}

The effect of R_{lm} is can be expressed by the leakage flux coefficient K_l, which is defined as Equation (4) [29]:

$$K_l = \frac{\Phi_g}{\Phi_m} = \frac{\Phi_g}{\Phi_g + \Phi_{lm}} \tag{4}$$

The MEC in Figure 1b is solved with respect to Φ_m, substituted into Equation (4), and then the equation is rearranged to give the OCAF:

$$\Phi_g = K_l \Phi_m = K_l \frac{R_{m2}}{R_{m2} + K_r R_g} \Phi_{r2} \tag{5}$$

After substituting $\Phi_r = A_m B_r$ into Equation (2) and rearranging the equations, the OCAF and its flux density are finally expressed by Equations (6) and (7), respectively:

$$\Phi_g = \frac{K_l A_m B_r}{1 + \frac{\mu_r l_{mg}}{l_m} + \frac{\mu_r K_r K_\phi K_c l_g}{l_m}} \tag{6}$$

$$B_g = \frac{K_l K_\phi B_r}{1 + \frac{\mu_r l_{mg}}{l_m} + \frac{\mu_r K_r K_\phi K_c l_g}{l_m}} \tag{7}$$

Here, K_ϕ is the concentration coefficient defined as A_m / A_g in SPM motor [29], in which A_m and A_g are the cross-sectional area of the magnet and airgap, respectively.

It can be known that $\mu_r l_{mg} / l_m$ is added to the denominator of Equation (6) when taking into account the additional airgap of the PM, as compared with what was written in [29] which did not

consider the additional airgap of the PM. The effect of the l_{mg} is similar to that of the l_g, as expressed in Equation (6); thus, its effect can be included and simulated by the l_g.

Figure 3 shows the flux ratio (FR) Φ_g/Φ_r as a function of magnet thickness-to-airgap length ratio l_m/l_g with respect to four parameters, i.e., l_{mg}/l_g, K_r for expressing l_{cg}, K_ϕ and K_l. As shown in Figure 3a–c, FRs become more robust against the variations of l_{mg}/l_g, K_r and K_ϕ as l_m/l_g increases, respectively. On the other hand, FR becomes more sensitive against variation of K_l as l_m/l_g increases and its small variation results in larger variation of the OCAF as compared to the previous parameters as shown in Figure 3d.

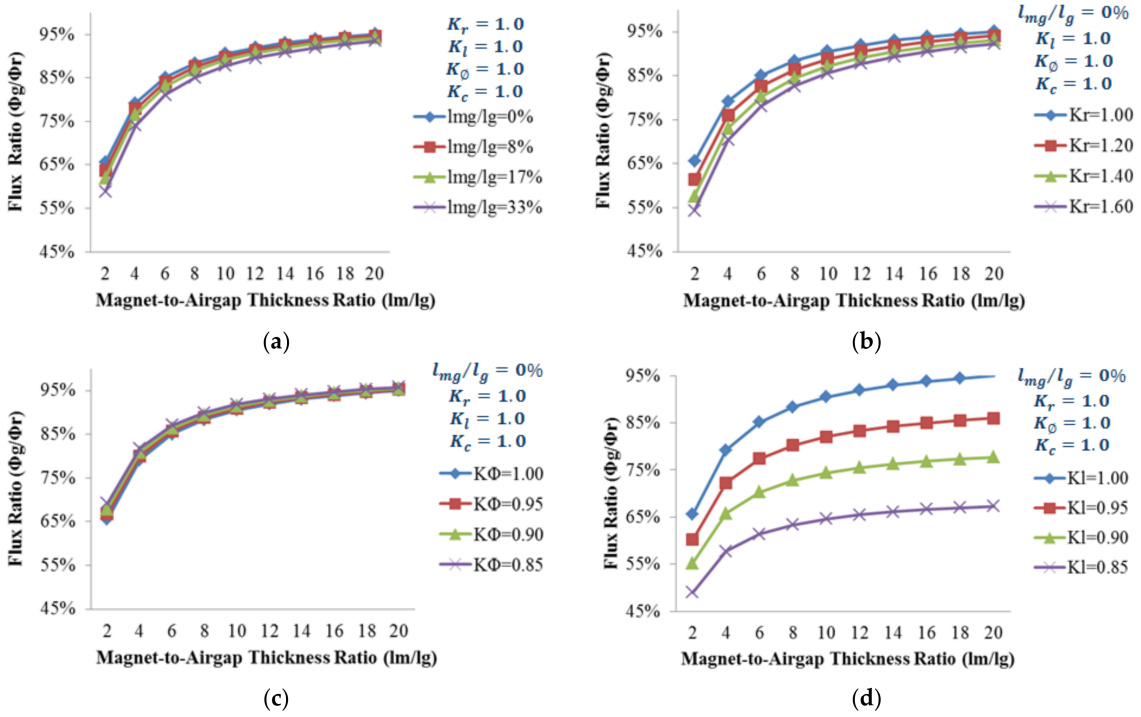

Figure 3. Effects of additional airgaps and design coefficients on the flux ratio: (**a**) Effect of the l_{mg}/l_g; (**b**) Reluctance coefficient; (**c**) Flux concentration coefficient; (**d**) Leakage flux coefficient.

Figure 4a shows the distributions of the OCAF density analyzed by the FEM according to the airgap lengths with l_m = 8.8 mm, l_{mg} = 0.2 mm, and MPA $\theta_m = 34.2°$, in which the slotless stator core is used for the analysis. It can be seen that an increasing airgap length results in a little increased leakage and fringing fluxes at the edge of the PMs as well as a decrease in the average OCAF; this means that the leakage flux coefficient K_l depends on the airgap length. In this paper, K_l is assumed to be constant in order to simplify the analysis.

Figure 4b compares distributions of OCAF densities with airgap lengths = 0.2 mm and 1.0 mm, analyzed by the FEM and MEC method in which $K_r = K_c = K_l = 1.0$, and $K_\phi = 0.845$ on the surface of the PM, respectively. As can be seen, there are differences between the FEM and the MEC results at the rising-edge (A) and the falling-edge (B). Both errors cancel each other out, reducing the error between FEM and MEC. The maximum errors of the peak and average OCAF densities between the FEM and MEC method are 1.8% and 3.7%, respectively.

Figure 5a shows the distributions of the OCAF densities analyzed by using the FEM as a function of the MTs with l_g = 0.6 mm, l_{mg} = 0.2 mm, and $\theta_m = 34.2°$. The variations of the flux densities according to the MTs are very small due to the high values of the permeance coefficients.

Figure 5b compares the distributions of the OCAF densities with magnet thicknesses = 6.8 mm and 10.8 mm, analyzed by the FEM and the MEC methods in which $K_r = K_c = K_l = 1.0$, and $K_\phi = 0.845$ on the surface of the PM, respectively. As can be seen, the differences between the FEM and the MEC

results at the rising-edge (A) and falling-edge (B) are similar to those of Figure 4b. The maximum errors of the peak and average OCAF densities between the FEM and MEC results are 1.5% and 4.8% in Figure 4b,c, respectively.

Figure 5c shows the distributions of the OCAF densities analyzed by using the FEM as a function of the MPA θ_m with l_g = 0.6 mm, l_m = 8.8 mm, and l_{mg} = 0.2 mm. Increasing the MPA results in a wider flat region and an almost constant fringing region in the OCAF density; thus, the leakage coefficient shows little variation, and it is assumed to be constant in this study.

Figure 5d compares the distributions of OCAF densities with MPA = 26.2○ and 42.2○, as analyzed by the FEM and MEC methods in which $K_r = K_c = K_l = 1.0$, and $K_\phi = 0.845$ on the surface of the PM, respectively. As can be seen, the differences between the FEM and the MEC results at the rising-edge (A) and the falling-edge (B) are also similar to those in Figure 5b. The maximum errors of the peak and average OCAF densities between the FEM and MEC method are 1.2% and 4.1%, respectively.

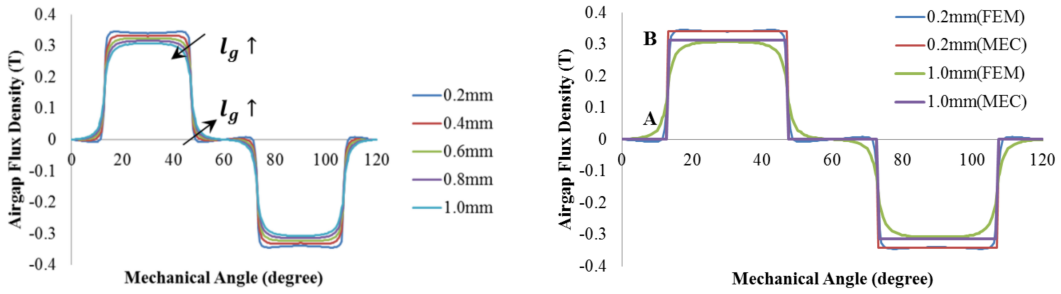

Figure 4. Effect of the airgap length on the open-circuit airgap flux (OCAF) density and comparison between the finite element method (FEM) and the MEC; (**a**) OCAF densities; (**b**) Comparison between the FEM and the MEC.

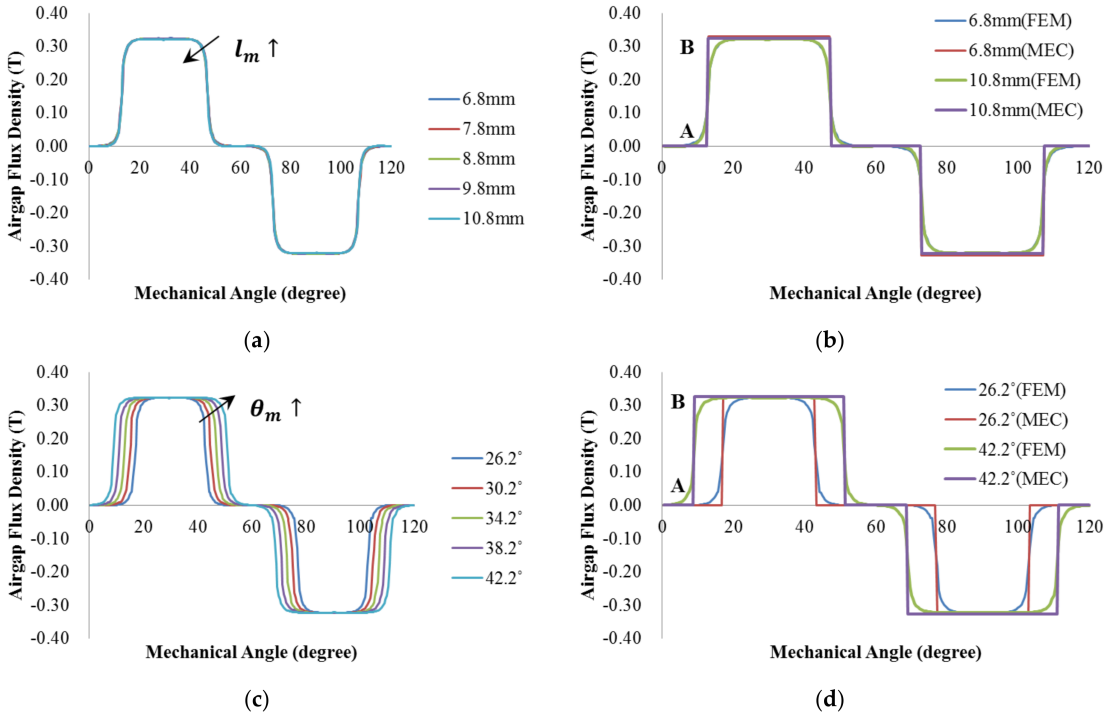

Figure 5. Effects of magnet thickness (MT) and magnet pole angle (MPA) on the OCAF density and a comparison between the FEM and the MEC results; (**a**) Effect of MT (FEM); (**b**) Comparison of the OCAF densities according to analysis methods (variable MT); (**c**) Effect of MPA (FEM); (**d**) Comparison of the OCAF densities according to analysis methods (variable MPT).

2.3. Tolerance Sensitivity Analysis Using Partial Derivative Method

By performing the tolerance sensitivity analysis before carrying out the robust optimal design, we can efficiently investigate the effects of design variables on a response Y, so that it helps us save the design cost and time. In this paper, the partial derivative method is used to analyze effects of design variables on the OCAF.

In general, the sensitivity using the partial derivative method is defined in Equation (8):

$$S = \frac{\partial y}{\partial x} \tag{8}$$

Here, y is a response and x is a design variable. Equation (9) shows that a smaller magnitude of the sensitivity results in less variation of the response y against a variable x.

Assuming that all variables are independent on the l_g, the sensitivity of the OCAF with respect to the airgap length is expressed as follows:

$$S = \frac{\partial \Phi_g}{\partial l_g} = -\frac{K_l K_r \mu_r K_\phi K_c A_m B_r}{l_m \left[1 + \frac{\mu_r l_{mg}}{l_m} + K_r \frac{\mu_r K_\phi K_c l_g}{l_m}\right]^2} \tag{9}$$

From Equations (8) and (9), some variables such as A_m, K_l, K_r, K_ϕ and K_c can be deployed into more detail design variables if necessary. In this paper, the three highly significant design variables, i.e., the airgap length, MT, MPA on the OCAF and its variation are investigated in detail.

Figure 6 shows the airgap fluxes and their sensitivities according to the airgap length, MT, MPA, and the same magnet volume condition.

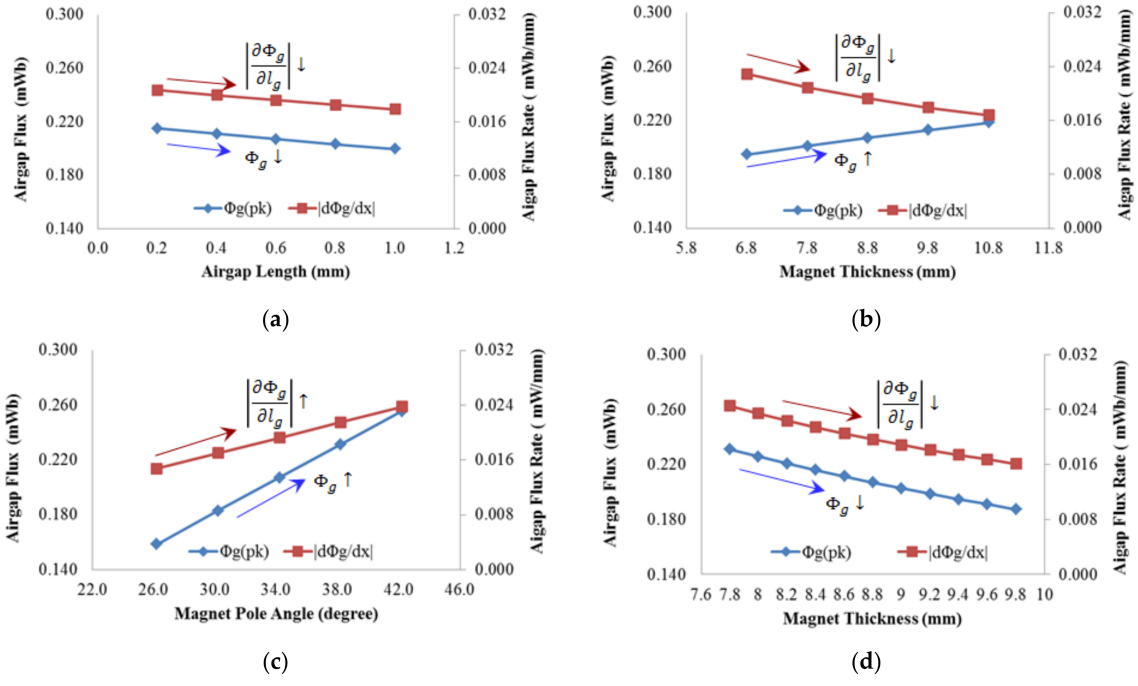

Figure 6. OCAFs and sensitivities with respect to design variables; (**a**) Airgap length; (**b**) Magnet thickness; (**c**) Magnet pole angle; (**d**) Same magnet volume condition.

As the airgap length increases, both the OCAF and its sensitivity decrease, as shown in Figure 6a. Increase of the magnet length results in an increased OCAF and a decreased sensitivity, as shown in Figure 6b. As shown in Figure 6c, both the OCAF and its sensitivity increase as the MPA increases.

A favorable design increases the OCAF and decreases its sensitivity; thus, increasing the MT is the simplest way to achieve these two goals simultaneously if the motor cost is not considered.

To take cost of magnet into account, the relation between l_m and MPA θ_m, related to the magnet volume of the SPM motor, can be expressed as shown below:

$$V_{mag} = \frac{N_p L_z \theta_m}{2}\left(l_m^2 + 2r_{mi}l_m\right) \tag{10}$$

Here, V_{mag} is the volume of the PMs and r_{mi} is the inside radius of PMs. Figure 6d shows the OCAF and its sensitivity with respect to the MT, with the same magnet volume satisfying Equation (10), whose results are similar to that in Figure 6a and different from that in Figure 6b. Thus, we should optimize the magnet volume considering trade-off between performance, i.e., mean and standard deviation, and cost. From the results of the analysis, it is known that increasing the MT is effective for both increasing the mean of the OCAF and reducing its variation

3. Robust Optimal Design of the OCAF Using Hybrid Response Surface Method

The objective of the (deterministic) optimal design is to maximally improve mean value μ_y of a response Y and, on the other hand, the robust design is to maximize robustness or to minimize its variation, e.g., standard deviation σ_y in the quality control.

The Taguchi robust design method has been widely used for improving robustness of the target response by considering uncontrollable noise factors such as manufacturing tolerances, temperature variation, etc. [13,14,16]. Taguchi robust design determines the robustness by using the signal-to-noise ratio (SNR) which is the robustness index expressed by the mean and standard deviation of the response.

However, SNR seems to have some demerits for the robust optimal design; it does not directly provide us with both the regression equation for investigating functional relationship between design variables and a response and the POF which is the ultimate goal index in the quality control.

In order to compensate for the demerits of SNR, this paper presents the H-RSM which is the hybrid of response surface method (RSM) and Taguchi robust design and directly finds the optimal point in terms of Z-value instead of SNR by using the regression equation because the target POF can be directly estimated by its corresponding Z-value [1]. Table 3 shows some important characteristics of the Z-value and SNR.

Table 3. Summary of the Z-value and signal-to-noise ratio (SNR).

Item		Z-Value	SNR
Equations according to response characteristics	Small-the-better	$Z_{bench} = Z_{USL} = \frac{USL-\mu}{\sigma}$	$SNR = -10log_{10}(\frac{1}{n}\sum_{i=1}^{n} y_i^2)$
	Larger-the-better	$Z_{bench} = Z_{LSL} = \frac{\mu-LSL}{\sigma}$	$SNR = -10log_{10}(\frac{1}{n}\sum_{i=1}^{n} \frac{1}{y_i^2})$
	Nominal-the-best	$Z_{Bench} = \Phi^{-1}\{\Phi(Z_{LSL}) + \overline{\Phi}(Z_{USL})\}$	$SNR = 10log_{10}\frac{\mu^2}{\sigma_i^2}$
Used method		H-RSM	Taguchi method
Design direction		Maximized	Maximized
Possibility to estimate POF		Possible (Absolute value)	Impossible (Relative value)
Optimization index		Possible	Impossible
Comparability between different responses in terms of POF		Possible	Impossible

Figure 7a shows the distributions of the responses according to means and standard deviations or Z-values, where SL is the specification limit and there are two SLs i.e., the lower SL (LSL) and the upper SL (USL). In Figure 7a, the LSL is used for the Z-value. It can be said that the robust optimal design has been successfully performed when Z-value is larger than 6.0 in the six-sigma process [1].

Figure 7b shows the difference between the conventional RSM and H-RSM, in which the H-RSM considers the variation of design variables and response caused by those of uncontrollable noise factors.

Figure 7c shows a flow chart of the robust optimal design procedure including the H-RSM used in this paper. To optimize the response considering the variation of the OCAF caused by those of the airgap lengths, the H-RSM uses the similar optimization procedure with that of the conventional RSM [34] except for using the orthogonal array composed of control and noise factors used in the Taguchi robust design and using the statistic values of the response instead of the response itself; the statistic values are mean, standard deviation, and Z-value.

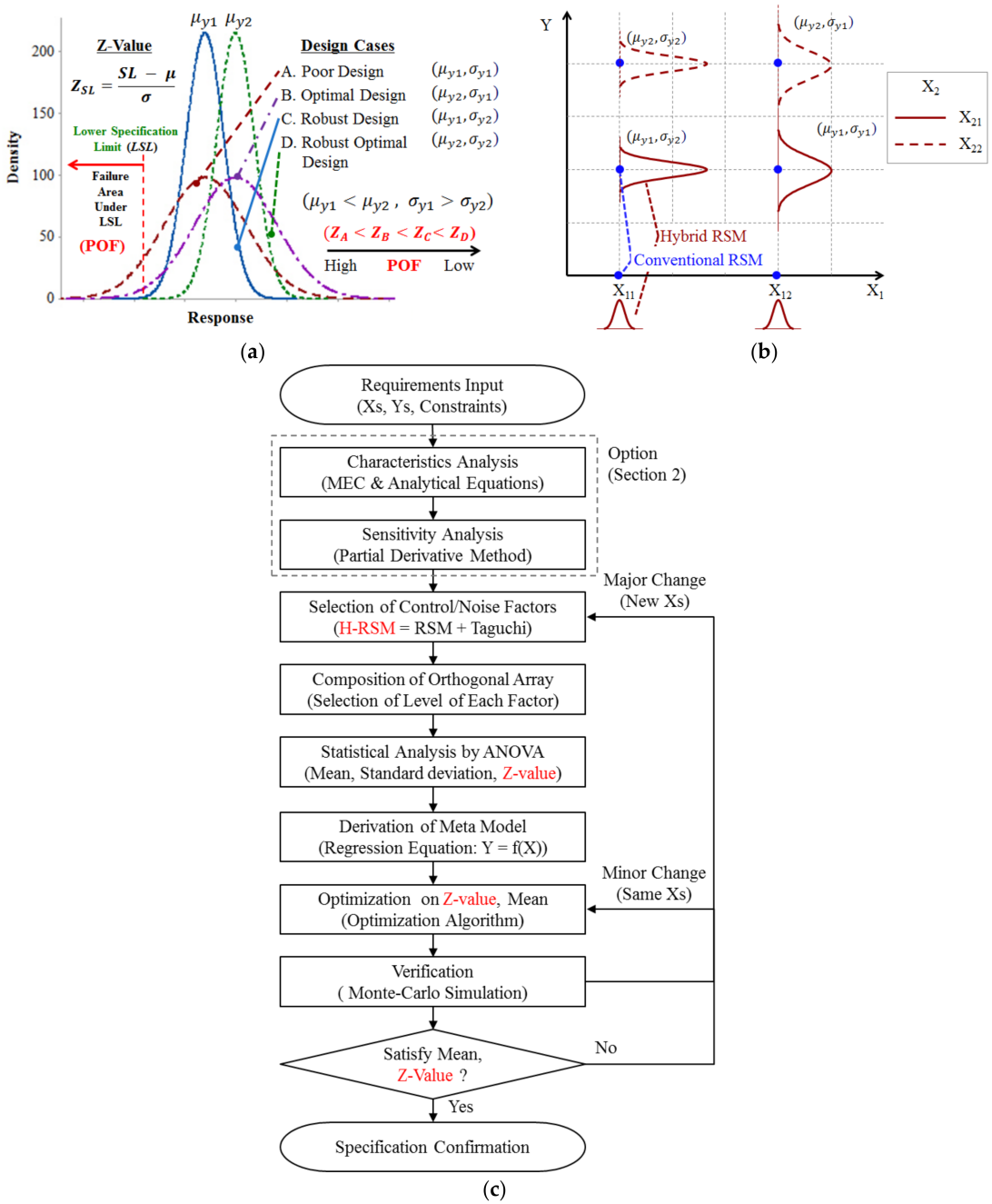

Figure 7. Robust optimal design by using the hybrid response surface method (H-RSM); (**a**) Distributions of responses according to Z-values resulted from different means and standard deviations; (**b**) Comparison of responses by using H-RSM to those of the conventional response surface method (RSM); (**c**) Flow chart of the optimal robust design using H-RSM.

In addition, the H-RSM directly finds the optimal point for achieving the six-sigma level of Z-value which is inversely proportional and in one-to-one correspondence to the POF, thus, it is more valid than SNR for estimating POF. Referring to Figure 7c, the following subsection provides a detailed description of the robust optimal design procedure.

3.1. Robust Optimal Design Using the Hybrid Response Surface Method and FEM

In the previous section, we used MEC and its analytical equation of the OCAF for studying the trends of the OCAF according to the design variables. For the robust optimal design, we use FEM modeled by the slotted stator core to consider slots and saturation effects. Let us carry out the design procedure referring to Figure 7c.

First, the objectives and constraint conditions of the H-RSM are described below:

$$\begin{aligned} &\text{Objectives}: \text{Maximize } \left[\mu(\Phi_g),\ Z_{LSL}(\Phi_g)\right] \\ &\qquad\quad \text{Maximize } V_{mag} \\ &\text{s.t.} \mu(\Phi_g) \geq 0.205 \text{ mWb} \\ &\quad Z_{LSL}(\Phi_g) \geq 6.0,\ \text{LSL}(\Phi_g) = 0.197 \text{ mWb} \\ &\quad 8.8 \text{ mm} \leq l_m \leq 10.8 \text{ mm} \\ &\quad 34.2 \leq \theta_m \leq 44.2\ ^\circ \\ &\quad \mu(l_g) = 0.6 \text{ mm}, \sigma(l_g) = 0.1 \text{ mm},\ 0.4 \text{ mm} \leq l_g \leq 0.8 \text{ mm} \end{aligned} \tag{11}$$

Here, the distribution of the airgap length satisfies the normal distribution conditions, i.e., $l_g \sim N(\mu_{l_g}, {\sigma_{l_g}}^2)$.

Second, Table 4 shows the control and noise factors on the OCAF used in the H-RSM, in which the controllable design factors are the MT and MPA and the airgap length is chosen as a noise factor, since it is the interesting and significant manufacturing tolerances on the OCAF.

Table 4. Control and noise factors on the OCAF used for the H-RSM.

Variable	Classification (Control/Noise Factor)	Level	
		1	**2**
A: MT	C	8.8	10.8
B: MPA	C	34.2	44.2
C: l_g	N satisfying Equation (11)	0.60 0.67 0.45 0.74 0.63 0.49 0.51 0.54 0.65 0.65 0.55	

Third, the H-RSM in this paper uses the orthogonal array in Table 5 and each combination performs Equation (11) trials same as the number of variations of the airgap length. The effects of the additional airgaps are assumed to be included in that of the airgap as was known in Equations (6) and (9). Table 5 shows a resultant orthogonal array structure for the H-RSM using data in Table 4.

Table 5. Orthogonal array structure for the H-RSM.

Control Factor		Noise Factor						Statistics		
		Response								
A	B	C_1	C_2	C_3	...	C_{n-1}	C_n	μ	σ	Z
A_1	B_1	$Y_{1,1}$	$Y_{1,2}$	$Y_{1,3}$	...	$Y_{1,n-1}$	$Y_{1,n}$	$\mu_{1,1}$	$\sigma_{1,1}$	$Z_{1,1}$
A_1	B_2	$Y_{2,1}$	$Y_{2,2}$	$Y_{2,3}$	...	$Y_{2,n-1}$	$Y_{2,n}$	$\mu_{1,2}$	$\sigma_{1,2}$	$Z_{1,2}$
A_2	B_1	$Y_{3,1}$	$Y_{3,2}$	$Y_{3,3}$	...	$Y_{3,n-1}$	$Y_{3,n}$	$\mu_{2,1}$	$\sigma_{2,1}$	$Z_{2,1}$
A_2	B_2	$Y_{4,1}$	$Y_{4,2}$	$Y_{4,3}$	...	$Y_{4,n-1}$	$Y_{4,n}$	$\mu_{2,2}$	$\sigma_{2,2}$	$Z_{2,2}$

Fourth, the regression equations of the statistic values of the OCAF are derived from the analysis of the response surface method as below:

$$\mu(\Phi_g) = 0.06781 + 0.002929 \times \text{MT} + 0.002367 \times \text{MPA} + 0.000102 \times \text{MT} \times \text{MPA} \quad (12)$$

$$\sigma(\Phi_g) = 0.001442 - 0.000021 \times \text{MT} + 0.000048\ \text{MPA} - 0.000001 \times \text{MT} \times \text{MPA} \quad (13)$$

$$Z(\Phi_g) = -48.35 + 1.703 \times \text{MT} + 0.8133 \times \text{MPA} + 0.02842 \times \text{MT} \times \text{MPA} \quad (14)$$

$$SNR(\Phi_g) = 0.3697 + 0.2633 \times \text{MT} + 0.1282 \times \text{MPA} - 0.000006 \times \text{MT} \times \text{MPA} \quad (15)$$

In the above equations, there are no quadratic terms because we used two levels of the MT and MPA as can be seen in Table 5; we should use three levels of a factor to include the quadratic terms of the factor. However, we think that the quadratic terms of MT and MPA have ignorable effect on the OCAF as can be seen in Figure 6. In addition, the three levels of a factor increase the number of cases to analyze than the two levels exponentially. Thus, we did not consider the quadratic terms in this paper. Next, the analyses using the regression equations are performed as follows.

Figure 8 shows the contour plots of the OCAF analyzed by using the data in Table 4. It is confirmed that the patterns of the mean and the sensitivity (which is proportional to the standard deviation) are similar to those obtained from the tolerance sensitivity analysis in Section 3.1; increased MT results in a smaller sensitivity as well as a higher mean of the OCAF, so the robustness against variations of the airgap length can be improved.

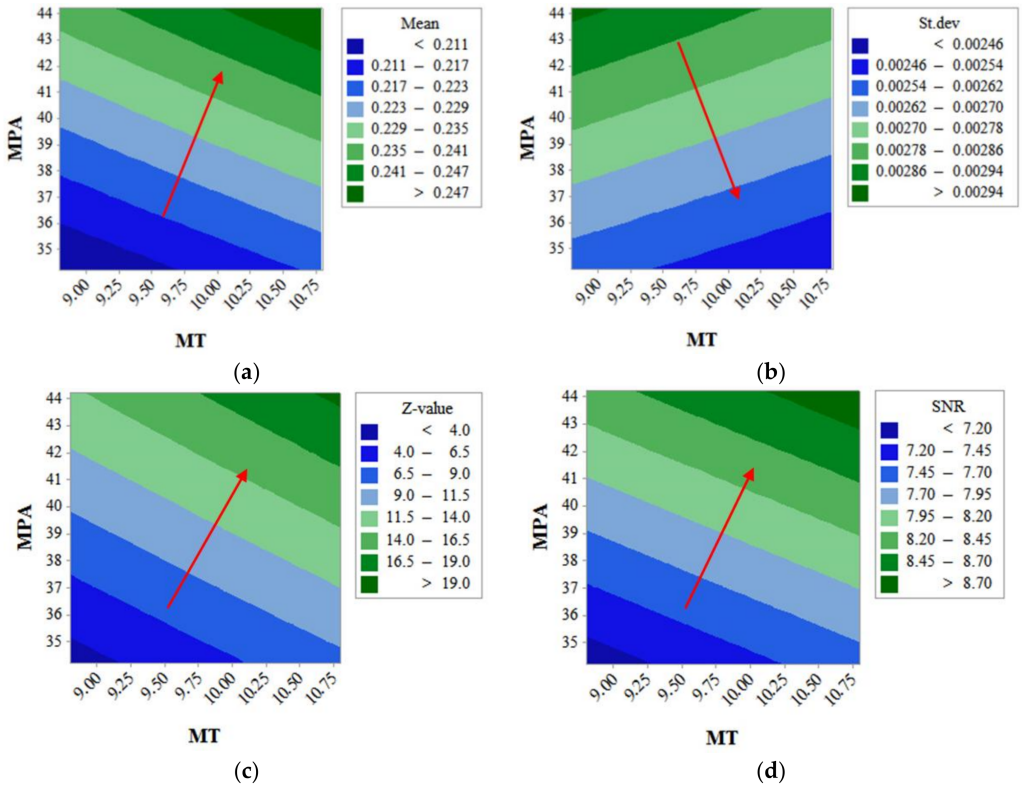

Figure 8. Contour plots of mean, standard deviation, Z-value, and optimal point; (**a**) Mean; (**b**) Standard deviation; (**c**) Z-value; (**d**) SNR.

The Z-value in Figure 8c and the SNR in Figure 8d are proportional to both the MT and MPA; investigating the convertibility between the Z-value and the SNR for estimating POF, it seems to be overall similar, but, not exactly the same. Thus, we should carefully use the SNR for reducing POF and it can be more valid and easy to use the Z-value rather than the SNR directly.

Lastly, the optimization is carried out using the regression equations to satisfy all objectives and constraints described in Equation (11).

Figure 9 shows the optimization result using the overlaid contour plot to find the optimal point satisfying Equation (11), in which the initial point moved to the optimal point from MPA = 34.2° to 37° with the same MT, l_m = 9.0 mm including l_{mg} = 0.2 mm although increasing MT and MPA show an increase and decrease in the variation of the OCAF, respectively. This is due to the fact that increasing MPA is easier and cost-effective than increasing MT for a higher Z-value.

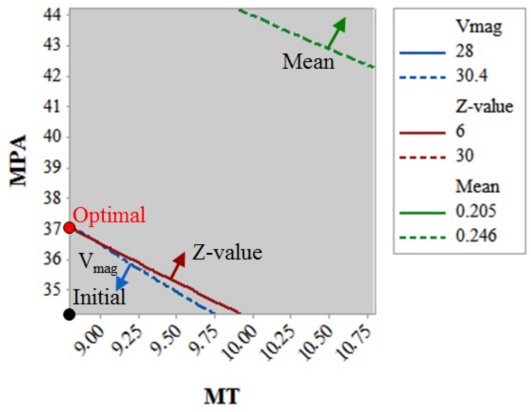

Figure 9. Optimal point using overlaid contour plot.

Figure 10a shows the waveforms of the airgap fluxes of the initial model and the optimal one and Figure 10b shows the waveforms of torques of the two models. It can be observed that the change is large as the absolute value increases.

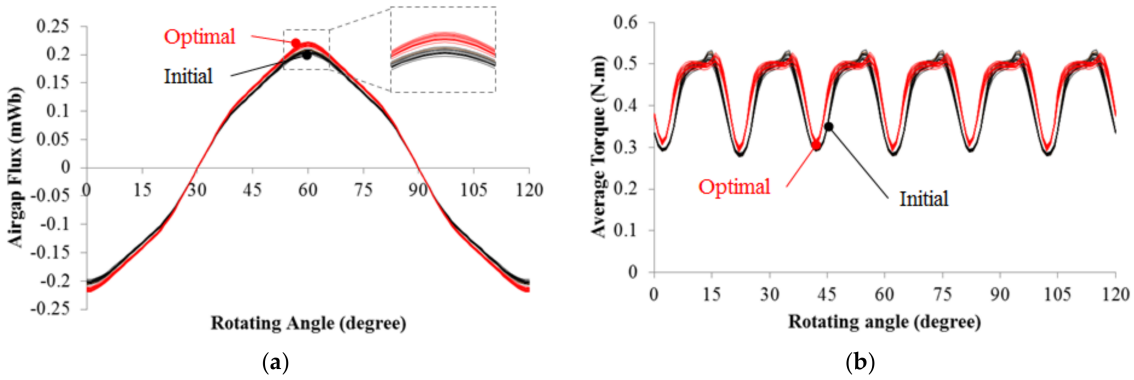

Figure 10. Comparison of optimal model to initial one; (**a**) Waveforms of airgap fluxes; (**b**) Waveforms of torques.

3.2. Verification of the Results Using the Monte-Carlo Simulation and FEM

In this section, the results of the tolerance sensitivity analysis obtained from the MEC in the previous section are verified by using the Monte-Carlo Simulation [1] and FEM.

Figure 11a shows the distributions of airgap fluxes according to the MT: l_m = 6.8, 8.8 and 10.8 mm at θ_m = 34.2°. It can be seen that the pattern of the airgap fluxes with respect to the magnet thicknesses coincides with that of Figure 6b, i.e., increased MT results in a higher μ_{Φ_g} and a lower σ_{Φ_g}.

Figure 11b shows distributions of the airgap fluxes according to the MPA: θ_m = 32.2°, 34.2° and 38.2° at the same other conditions. The pattern of the airgap fluxes with the MPA is also similar to that of Figure 6c; an increase in the MPA results in a higher μ_{Φ_g} and σ_{Φ_g}.

Figure 11c shows distributions of airgap fluxes according to the combination of magnet thicknesses and MPAs with the same PM volume and other conditions. It can be seen that the pattern of airgap fluxes with the same magnet volume coincides with that of Figure 6d; increasing MT and decreasing MPA result in both a lower μ_{Φ_g} and σ_{Φ_g}.

Figure 11d shows the distributions of airgap fluxes of the initial and optimal model. All of the results coincide with those of the tolerance sensitivity analysis and H-RSM.

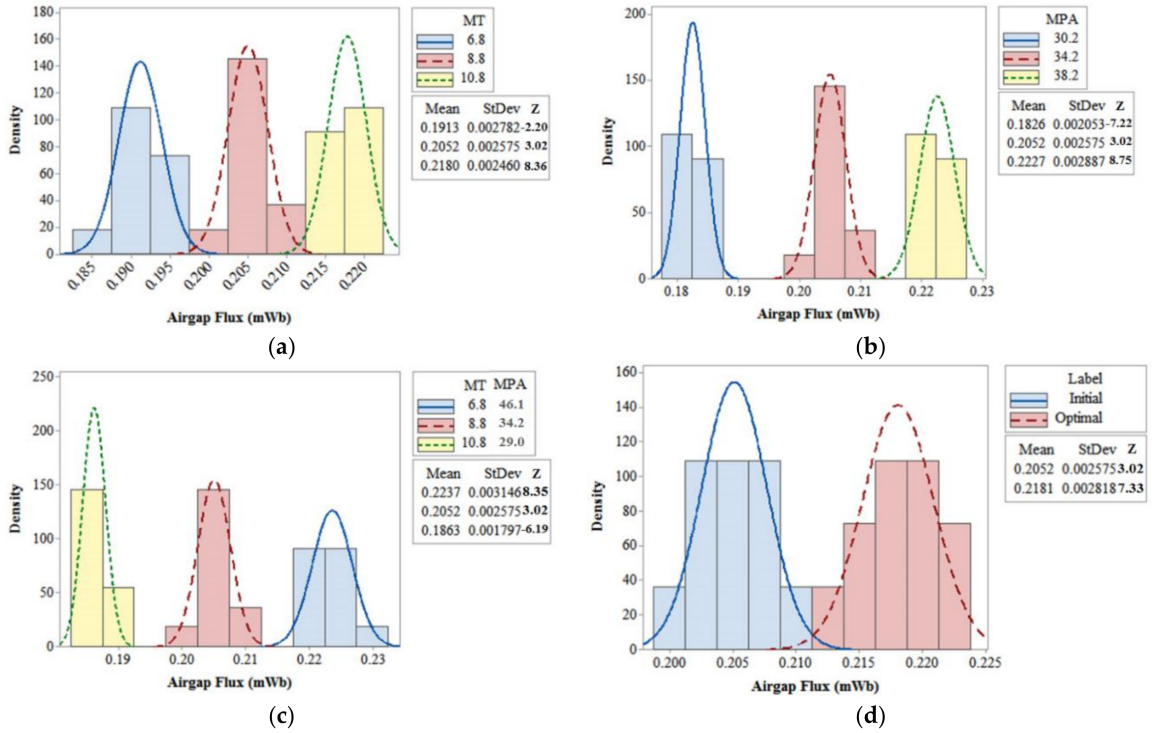

Figure 11. Distributions of the OCAFs according to design variables; (**a**) Magnet thickness; (**b**) Magnet pole angle; (**c**) Same magnet volume condition; (**d**) Comparison between initial and optimal model.

Table 6 shows the comparison of the optimal model to the initial model shown in Figure 8a. As can be seen, it can be observed that the Z value of the optimal model increased more than twice as much as the initial model.

Table 6. Comparison of the optimal model to the initial one.

Term		Unit	Value	
			Initial	Optimal
MT		mm	8.8	8.8
MPA		deg.	34.2	37.0
Magnet Volume		cm^3	28.0	30.3
OCAF	Mean	mWb	0.205	0.218
	Standard deviation	mWb	0.0026	0.0028
	Z-value	σ-level	3.0	7.3

4. Conclusions

Herein, the OCAF and its variation caused by the variations in the airgap length were investigated as a function of the main design variables such as airgap length, MT, and MPA. This was done by using the MEC and its induced equations, taking into consideration the additional airgap between the magnet and rotor back yoke.

The tolerance sensitivity analysis was carried out by the partial derivative method, from which we investigated the functional relationships between the design variables and the OCAF. The H-RSM, which is the hybrid of the RSM and Taguchi robust design and uses the Z-value instead of SNR as the robustness index, was suggested for the robust optimal design. It was shown that the Z-value is

more valid index than SNR for estimating POF because SNR is not always proportional to POF, i.e., not always in inverse proportional to the Z-value.

Finally, the results of the tolerance sensitivity analysis performed by the MEC and robust optimal design performed by H-RSM were verified by the FEM, and the results showed good agreement.

From the analysis results, it was confirmed that increasing the MT results in reducing variations of the OCAF due to those of the airgap length as well as increasing the mean of the OCAF. On the other hand, increasing the MPA results in increasing variations of the OCAF due to those of the airgap length as well as increasing the mean of the OCAF.

Therefore, motor designers should determine the dimensions of the MT and MPA considering the variance as well as the mean value of the OCAF to achieve the target probability of failure.

In their next study, the authors will study the improved robust design method for various motor types using MEC considering more practical issues or noise factors, e.g., the magnetic saturation effect, armature reaction effect, and so on.

Author Contributions: All the authors contributed substantially to the work presented. C.-S.J. carried out the simulations and analyzed the results. In addition, he wrote the paper. B.-I.K. gave advice and O.K. revised the manuscript.

Conflicts of Interest: The authors declare no conflict of interest.

References

1. Jun, C.S.; Kwon, B.I. Process Capability Control Procedure for Electrical Machines by Using a Six-Sigma Process for Achieving Six Sigma Quality Level. *IET Electr. Power Appl.* **2017**, *11*, 1466–1474. [CrossRef]
2. Islam, M.S.; Mir, S.; Sebastian, T. Issues in reducing the cogging torque of mass-produced permanent-magnet brushless DC motor. *IEEE Ind. Appl.* **2004**, *40*, 813–820. [CrossRef]
3. Islam, M.S.; Islam, R.; Sebastian, T.; Chandy, A.; Ozsoylu, S.A. Cogging Torque Minimization in PM Motors Using Robust Design Approach. *IEEE Ind. Appl.* **2011**, *47*, 1661–1668. [CrossRef]
4. Gasparin, L.; Cernigoj, A.; Markic, S.; Fiser, R. Additional cogging torque components in permanent-magnet motors due to manufacturing imperfections. *IEEE Trans. Magn.* **2009**, *45*, 1210–1213. [CrossRef]
5. Kitamura, M.; Enomoto, Y.; Kaneda, J.; Komuro, M. Cogging Torque Due to Roundness Errors of the Inner Stator Core Surface. *IEEE Trans. Magn.* **2003**, *39*, 1622–1625. [CrossRef]
6. Zhu, Z.Q.; Azar, Z.; Ombach, G. Influence of Additional Air Gaps Between Stator Segments on Cogging Torque of Permanent-Magnet Machines Having Modular Stators. *IEEE Trans. Magn.* **2012**, *48*, 2049–2055. [CrossRef]
7. Lee, T.Y.; Seo, M.K.; Kim, Y.J.; Jung, S.Y. Cogging Torque of Surface-mounted Permanent Magnet Synchronous Motor According to Segmented-Stator Core Effect. In Proceedings of the International Conference on Electrical Machine (ICEM), Lausanne, Switzerland, 4–7 September 2016; pp. 200–206. [CrossRef]
8. Kim, J.M.; Yoon, M.H.; Hong, J.P.; Kim, S.I. Analysis of cogging torque caused by manufacturing tolerances of surface-mounted permanent magnet synchronous motor for electric power steering. *IET Electr. Power Appl.* **2016**, *10*, 691–696. [CrossRef]
9. Guo, H.; Wu, Z.; Qian, H.; Yu, K.; Xu, J. Statistical analysis on the additional torque ripple caused by magnet tolerances in surface-mounted permanent magnet synchronous motors. *IET Electr. Power Appl.* **2014**, *9*, 183–192. [CrossRef]
10. Ortega, A.J.P.; Paul, S.; Islam, R.; Xu, L. Analytical Model for Predicting Effects of Manufacturing Variations on Cogging Torque in Surface-Mounted Permanent Magnet Motors. *IEEE Trans. Ind. Appl.* **2016**, *52*, 3050–3061. [CrossRef]
11. Ortega, A.J.P.; Xu, L. Analytical Prediction of Torque Ripple in Surface-Mounted Permanent Magnet Motors Due to Manufacturing Variations. *IEEE Trans. Energy Conv.* **2016**, *31*, 1634–1644. [CrossRef]
12. Heins, G.; Brown, T.; Thiele, M. Statistical Analysis of the Effect of Magnet Placement on Cogging Torque in Fractional Pitch Permanent Magnet Motors. *IEEE Trans. Magn.* **2011**, *47*, 2142–2148. [CrossRef]
13. Chowdhury, M.; Islam, M.; Gebregergis, A.; Sebastian, T. Robust design optimization of permanent magnet synchronous machine utilizing genetic and Taguchi's algorithm. In Proceedings of the Energy Conversion Congress and Exposition (ECCE), Denver, CO, USA, 15–19 September 2013; pp. 5006–5012. [CrossRef]

14. Lee, S.J.; Kim, J.M.; Cho, S.J.; Jang, J.; Lee, T.; Hong, J. Optimal design of interior permanent magnet synchronous motor considering the manufacturing tolerances using Taguchi robust design. *IET Electr. Power Appl.* **2014**, *8*, 23–28. [CrossRef]
15. Guo, H.; Wu, Z.; Qian, H.; Sun, Z. Robust design for the 9-slot 8-pole surface-mounted permanent magnet synchronous motor by analytical method-based multi-objectives particle swarm optimization. *IET Electr. Power Appl.* **2016**, *10*, 117–124. [CrossRef]
16. Kim, K.S.; Jung, K.T.; Kim, J.M.; Hong, J.P.; Kim, S.I. Taguchi robust optimum design for reducing the cogging torque of EPS motors considering magnetic unbalance caused by manufacturing tolerances of PM. *IET Electr. Power Appl.* **2016**, *10*, 909–915. [CrossRef]
17. Krasopoulos, C.T.; Beniakar, M.E.; Kladas, A.G. Robust Optimization of High-Speed PM Motor. *IEEE Trans. Magn.* **2017**, *53*, 7207304. [CrossRef]
18. Lee, J.G.; Hwang, N.W.; Ryu, H.R.; Jung, H.K.; Woo, D.K. Robust Optimization Approach Applied to Permanent Magnet Synchronous motor. *IEEE Trans. Magn.* **2017**, *53*, 8001804. [CrossRef]
19. Khan, M.A.; Husain, I.; Islam, M.R.; Klass, J. Design of Experiments to Address Manufacturing Tolerances and Process Variations Influencing Cogging Torque and Back EMF in the Mass Production of the Permanent-Magnet Synchronous Motors. *IEEE Trans. Ind. Appl.* **2014**, *50*, 346–355. [CrossRef]
20. Kim, Y.S; Sul, S.K. Torque Control Strategy of an IPMSM Considering the Flux Variation of the Permanent Magnet. In Proceedings of the IAS Annual Meeting, New Orleans, LA, USA, 23–27 September 2007; pp. 1301–1307. [CrossRef]
21. Lei, G.; Guo, Y.G.; Zhu, J.G.; Wang, T.S.; Chen, X.M.; Shao, K.R. System Level Six Sigma Robust Optimization of a Drive System with PM Transverse Flux Machine, Sigma. *IEEE Trans. Magn.* **2012**, *48*, 923–926. [CrossRef]
22. Lei, G.; Zhu, J.G.; Guo, Y.G.; Hu, J.F.; Xu, W.; Shao, K.R. Robust design optimization of PM-SMC motors for six sigma quality manufacturing. *IEEE Trans. Magn.* **2013**, *49*, 3953–3956. [CrossRef]
23. Lei, G.; Zhu, J.G.; Guo, Y.G.; Shao, K.; Xu, W. Multiobjective Sequential Design Optimization of PM-SMC Motors for Six Sigma Quality Manufacturing. *IEEE Trans. Magn.* **2014**, *50*, 7017704. [CrossRef]
24. Lei, G.; Wang, T.; Zhu, J.; Guo, Y.; Wang, S. System-Level Design Optimization Method for Electrical Drive Systems—Robust Approach. *IEEE Trans Ind. Electron.* **2015**, *62*, 4702–4713. [CrossRef]
25. Ma, B.; Lei, G.; Liu, C.; Zhu, J.; Guo, Y. Robust Tolerance Design Optimization of a PM Claw Pole Motor With Soft Magnetic Composite Cores. *IEEE Trans. Magn.* **2018**, *54*, 8102404. [CrossRef]
26. Ma, B.; Lei, G.; Zhu, J.; Guo, Y.; Liu, C. Application-Oriented Robust Design Optimization Method for Batch Production of Permanent-Magnet Motors. *IEEE Trans. Ind. Elec.* **2018**, *65*, 1728–1739. [CrossRef]
27. Putek, P.A.; Maten, E.J.W.; Günther, M.; Sykulski, J.K. Variance-Based Robust Optimization of a Permanent Magnet Synchronous Machine. *IEEE Trans. Magn.* **2018**, *54*, 8102504. [CrossRef]
28. Tian, Z.; Zhang, C.; Zhang, S. Analytical Calculation of Magnetic Field Distribution and Stator Iron Losses for Surface-Mounted Permanent Magnet Synchronous Machines. *Energies* **2017**, *10*, 320. [CrossRef]
29. Hanselman, D. *Brushless Permanent Magnet Motor Design*, 2nd ed.; The Writers' Collective: Cranston, RI, USA, 2003; pp. 24–28, 68–72, ISBN 1932133631.
30. Qu, R.; Lipo, T.A. Analysis and Modeling of Air-Gap and Zigzag Leakage Fluxes in a Surface-Mounted Permanent-Magnet Machine. *IEEE Trans. Ind. Appl.* **2004**, *40*, 121–127. [CrossRef]
31. Yeo, H.K.; Lim, D.K.; Woo, D.K.; Ro, J.S.; Jung, H.K. Magnetic Equivalent Circuit Model Considering Overhang Structure of a Surface-Mounted Permanent-Magnet Motor. *IEEE Trans. Magn.* **2015**, *51*, 8201004. [CrossRef]
32. Feng, Y.I.; Zhang, C. Analytical Calculation for Predicting the Air Gap Flux Density in Surface-Mounted Permanent Magnet Synchronous Machine. *J. Electr. Eng. Technol.* **2017**, *12*, 769–777. [CrossRef]
33. Song, J.Y.; Lee, J.H.; Kim, D.W.; Kim, Y.J.; Jung, S.Y. Analysis and Modeling of Concentrated Winding Variable Flux Memory Motor Using Magnetic Equivalent Circuit Method. *IEEE Trans. Magn.* **2017**, *53*, 8102704. [CrossRef]
34. Myers, R.H.; Montgomery, D.C.; Anderson-cook, C.M. *Response Surface Methodology*, 3rd ed.; A JOHN WILEY & SONS, Inc.: Hoboken, NJ, USA, 2008; pp. 1–9, ISBN 978-0-470-17446-3.